

Application of the PIV technique to measurements around and inside a forming drop in a liquid–liquid system

Anna Timgren · Gun Trägårdh · Christian Trägårdh

Received: 5 July 2006 / Revised: 5 September 2007 / Accepted: 5 October 2007 / Published online: 23 October 2007
© Springer-Verlag 2007

Abstract A particle image velocimetry (PIV) method has been developed to measure the velocity field inside and around a forming drop with a final diameter of 1 mm. The system, including a microscope, was used to image silicon oil drops forming in a continuous phase of water and glycerol. Fluorescent particles with a diameter of 1 μm were used as seeding particles. The oil was forced through a 200 μm diameter glass capillary into a laminar cross-flow in a rectangular channel. The velocity field was computed with a double-frame cross-correlation function down to a spatial resolution of $21 \times 21 \mu\text{m}$. The method can be used to calculate the shear stress induced at the interface by the cross-flow of the continuous phase and the main forces involved in the drop formation process.

1 Introduction

The formation of one drop of liquid in another, immiscible, liquid is of great interest in many applications since this occurs in several chemical processes. Examples are chemical reactions, combustion and emulsification processes, especially microchannel and membrane emulsification. In this paper, studies of the formation of an oil drop from a single glass capillary in a liquid flowing perpendicular to the capillary opening is described. The process can be divided in two main steps: (1) drop formation, as the dispersed phase is forced out of the capillary and the drop

grows at the capillary opening, and (2) detachment, when the drop detaches from the dispersed phase and moves with the continuous phase, which is flowing tangentially to the capillary opening. The forces acting on a drop determine the drop formation and detachment, and are described as follows (Peng and Williams 1998; Wang et al. 2000; Xu et al. 2005).

The cross-flow of the continuous phase has a considerable viscous effect in the process since the shear stress and pressure gradient resulting from the continuous phase influence the forming drop, causing a drag force (F_D) promoting drop detachment,

$$F_D = 3k_x \pi \mu_{\text{cont}} d_{\text{drop}} u_c \left(\frac{1 + \frac{2}{3}\kappa}{1 + \kappa} \right) \quad (1)$$

where

- k_x is 1.7, a correction factor for a sphere at a wall (O'Neill 1968),
- κ is the ratio of the viscosity of the continuous to that of the dispersed phase,
- μ_{cont} is the viscosity in the continuous phase,
- d_{drop} is the diameter of the drop, and
- u_c is the undisturbed tangential velocity of the continuous phase at the drop centre.

Other forces that can be considered to promote detachment are the lift force (F_L),

$$F_L = 0.761 \frac{\tau_w^{1.5} d_{\text{drop}}^3 \rho_{\text{cont}}^{0.5}}{\mu_{\text{cont}}} \quad (2)$$

the inertial force (F_I),

$$F_I = \frac{\pi}{4} \rho_{\text{disp}} u_{\text{disp}}^2 d_{\text{cap}}^2 \quad (3)$$

and the static pressure difference force (F_{SP})

A. Timgren (✉) · G. Trägårdh · C. Trägårdh
Department of Food Technology, Engineering and Nutrition,
Lund University, P.O. Box 124, 221 00 Lund, Sweden
e-mail: anna.timgren@food.lth.se

$$F_{SP} = \frac{\pi\gamma}{d_{\text{drop}}} d_{\text{cap}}^2 \quad (4)$$

where

- τ_w is the wall shear stress,
- ρ_{cont} is the density of the continuous phase,
- ρ_{disp} is the density of the dispersed phase,
- u_{disp} is the velocity of the dispersed phase out of the capillary,
- d_{cap} is the diameter of the capillary opening, and
- γ the surface tension.

The buoyancy force (F_B)

$$F_B = \Delta\rho g V_{\text{drop}} \quad (5)$$

where V_{drop} is the volume of the forming drop, will also promote detachment when the density of the dispersed phase is lower than the density of the continuous phase, since the difference in density is the cause of this force. The lift force results from the pressure distribution caused by the velocity gradient in the cross-flow acting on the forming drop; the inertial force is caused by the dispersed phase flow through the capillary as it inflates the drop; and the static pressure force is due to the difference in static pressures between the inside and outside of the forming drop at the capillary opening. A force that acts against detachment is the interfacial tension force (F_γ)

$$F_\gamma = \pi\gamma d_{\text{cap}} \quad (6)$$

the adhesion of the dispersed phase to the end of the capillary being the origin of this force. The drop detaches when the magnitude of the detaching forces exceeds the interfacial tension force. The main forces involved in drop formation and detachment are illustrated in Fig. 1a, and an estimate of the magnitude of all forces is shown in Fig. 1b. It can be seen that the drag and buoyancy forces have the greatest influence on drop detachment for a drop with a final diameter of approximately 1 mm.

In order to better understand the process some groups have visualised the formation and detachment of drops in

various systems, and they have used different techniques to obtain as accurate a picture as possible of the process. Peng and Williams (1998) used a single glass pore and a high-speed video camera to visualise droplet formation, and found that an increase in cross-flow velocity decreased the drop size and drop formation time, while the effects of increased oil pressure were less important. Kobayashi et al. (2002) used a polycarbonate membrane with uniform pores and visualised the process from above with a microscope video system including a metallographic microscope, a CCD camera and a video camera. Their results showed that a cross-flow was necessary to make the drops detach, and that the drop size decreased with increasing cross-flow velocity. The same group also used a membrane of Shirasu porous glass (SPG) (Miyazaki, Japan) for emulsification, and recorded the process from above with a high-speed camera (Yasuno et al. 2002). They found that the cross-flow velocity hardly affected the drop size and the drops were formed spontaneously, mainly because of the tortuous pore structure in the SPG membrane. Abrahamse et al. (2002) used a microengineered microsieve with uniform pores uniformly distributed over the membrane surface and visualised the formation of droplets from above with a microscope and a CCD video camera. They observed the formation of polydispersed drops and explained this by drop interaction and steric hindrance. The same group also studied droplet formation at a single microsieve pore with special emphasis on the surface tension (van der Graaf et al. 2004) and established that both drop size and drop formation time decreased with increasing surfactant concentration. Using a screen with square holes of 45 μm , Xu et al. (2005) studied the effects of flow rates and interfacial tension on droplet formation from above, and the results were found to be in good agreement with a theoretical model based on the force–torque balance.

A method of visualising and measuring the motion and velocity profiles around and inside a drop will provide new insight into the formation and detachment processes. A technique that could be used for this purpose is the particle

Fig. 1 **a** Schematic illustration of the drop formation process and the main forces involved. **b** Order of magnitude analysis of the forces acting on a forming drop at average velocities of 0.11 and 0.017 m/s in the continuous and dispersed phase, respectively. The fluid properties used are listed in Table 1

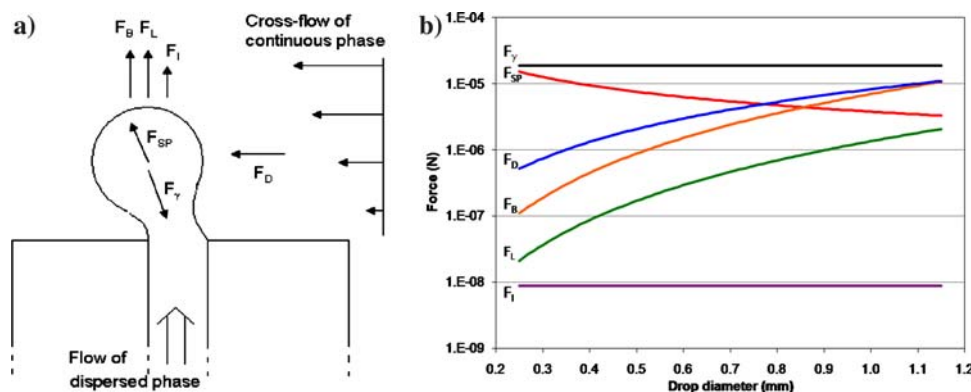


image velocimetry (PIV) method. PIV has not been applied to the investigation of velocity profiles during droplet formation and detachment on the scale studied here, but it has been used for other applications involving a two-phase system consisting of oil and water with matching refractive indices. Studies have been performed on the impact of a drop at an oil–water interface (Mohamed-Kassim and Longmire 2003, 2004) and the pinch-off modes in a glycerine/water jet flowing into silicon oil (Milosevic and Longmire 2002). Augier et al. (2003) used heptane as the dispersed phase in a water/glycerine solution to measure the velocities of the phases, the volume fractions and the size of the dispersed drops. Another system consisting of silicon oil as dispersed phase in an aqueous NaI continuous phase was used by Svensson and Rasmusen (2004) for experiments in a stirred vessel. PIV has been used for measurements in microfluidics by, among others, Santiago et al. (1998), Lindken et al. (2002), Koutsiaris et al. (1999) and Westerweel et al. (2004). In micro-PIV, an epifluorescent microscope is often used and the measurement volume is limited by the depth of focus of the imaging optics, and not by the thickness of the light sheet, as in conventional PIV.

The aim of this work was to develop a measurement technique that can be used to explain the physical phenomena occurring during drop formation. For this purpose, a modified PIV method was used to determine the velocity field inside and around an oil drop, during formation from a single glass capillary with an internal diameter of 200 μm , in a continuous phase of water and glycerol. Knowledge of the velocities is useful in understanding the shear stress at the interface between the two phases, and the influence of the forces involved on drop detachment and final drop size. The results obtained from this experimental study will also be valuable in validating numerical simulations of the drop formation process.

2 Materials and methods

2.1 Materials

The system of fluids consisted of a mixture of milli-Q water and glycerol (>98%, VWR International, Stockholm, Sweden) as the continuous phase, and silicon oil (DC200, also from VWR) as the dispersed phase. In order to obtain

matching refractive indices (1.401) between the two phases a mixture of water/glycerol with a volume ratio (v/v) of 0.54/0.46 and silicon oil with a kinematic viscosity of 0.50 cm^2/s were used (Mohamed-Kassim and Longmire 2003). The fluid properties are given in Table 1. The data for the density and viscosity of the liquids are from the work by Mohamed-Kassim and Longmire (2003). The uncertainty for the interfacial tension depends on the variation during the first seconds of the interfacial tension measurement, i.e. the time for drop formation.

Rhodamine-B-labelled melamine resin particles (microParticles GmbH, Berlin, Germany) with a diameter of 1.05 μm ($\pm 0.040 \mu\text{m}$) were used as seeding particles. This particle size was chosen because the image spot of the light scattered by these particles corresponds to 1–2 pixels, which is the optimum particle-image diameter according to Westerweel (2000). The particles have a density of 1510 kg/m^3 and a refractive index of 1.68. The estimated response time of these particles is 10 ns and, compared to the characteristic time of the flow, which is over 5 μs , it can be assumed that the particles follow the motion of the fluids with respect to Stokes number (Crowe et al. 1998). Since the particles are labelled with Rhodamine-B they are fluorescent and emit light at a wavelength of approximately 560 nm, with an emission peak at 584 nm. In the experiments, an aqueous dispersion of particles was used in the continuous phase or a dry powder in the dispersed phase, depending on the velocities measured (inside or around the drop). The concentration of particles was 3×10^{10} particles/l fluid, which gives a seeding density of at least 10 particles per interrogation area with a size of 32×32 pixels, and an estimated acceptable focal depth of 50 μm .

2.2 Flow system

Figure 2 shows a sketch of the experimental set-up for the flow system used in the study. The experiments were performed in a rectangular steel channel with a glass window to allow imaging, and a polymethyl methacrylate (PMMA) window for the laser illumination. The channel was 20 mm in width, 5 mm in height and 500 mm long to achieve a laminar profile in the measurement region. The continuous phase was pumped through the channel with a volumetric pump (316 Liquiflo, Warren, NJ, USA). The dispersed phase was kept in a container and forced by overpressure

Table 1 Properties of the fluids used in the system

Fluid	Density (kg/m^3)	Viscosity (mPa s)	Refractive index	Surface tension (mN/m)
Water/glycerol (0.54/0.46 v/v)	1,130	6.7	1.401 (± 0.0004)	29.5 (± 0.3)
Silicon oil DC200 50cSt	960	48		

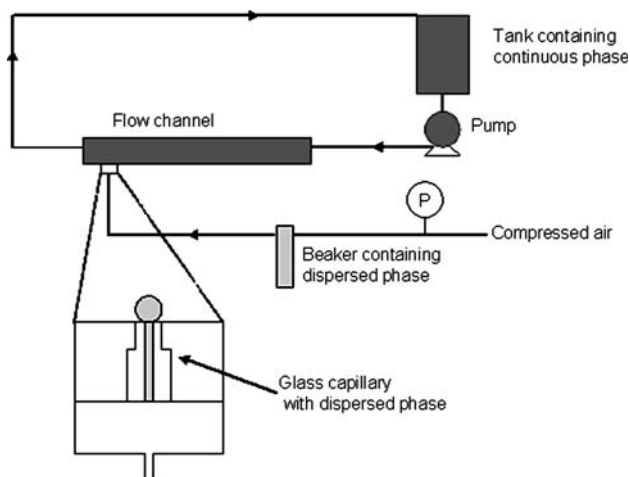


Fig. 2 Sketch of the experimental set-up of the flow system showing an enlargement of the region including the glass capillary

through a glass capillary with an inner diameter of 200 μm and a length of 15 mm. The oil in the capillary flowed into the centre at the bottom of the measurement region of the channel and drops were formed continuously. A constant pressure was applied to the oil phase; however the velocity in the capillary is affected by the pressure caused by the cross-flow in the channel and, above all, the pressure inside the forming drop. This pressure corresponds to the Laplace pressure, which is inversely proportional to the radius of the drop. This results in a large pressure not only at the beginning of the drop formation process, but also at the end when the neck has been formed. The studies were performed at a drop formation time of 1 drop/s, when the average velocity of the cross-flow was 0.11 m/s and the applied pressure was 90 kPa. The Reynolds number (Re) in the channel under these conditions was 155 and the Reynolds number in the capillary (Re_{cap}) was around 0.07, but varied slightly during the formation of a drop due to the variation in capillary velocity.

2.3 Visualisation system

The particles in the flow system were illuminated by a Nd:YAG double-pulsed laser (New Wave Research, Fremont, CA, USA) with a wavelength of 532 nm and a pulse

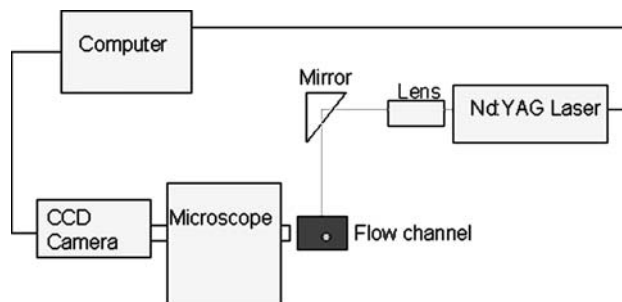


Fig. 3 Sketch of the experimental set-up of the visualisation system

width of about 5 ns. The laser beam was transformed into a sheet using an optical system (LaVision GmbH, Göttingen, Germany) and directed through the PMMA window of the channel. It was ensured that the light sheets originating from the two laser beams had identical intensity and position, and were parallel to the long axis of the channel. The illuminated particles were imaged perpendicular to the laser sheet using a CCD camera (Flowmaster 3, also from LaVision GmbH) attached to a microscope (BX30, Olympus, Tokyo, Japan). The visualisation system is illustrated in Fig. 3.

A long working distance objective (LMPlanFL $\times 5$, Olympus) was used with the microscope, and a $\times 0.5$ magnification adaptor was inserted between the microscope and the camera to give a total magnification of $\times 2.5$. A long-pass filter with a cut-off of 570 nm (03 FCG 498, Melles Griot, Carlsbad, CA, USA) was used to protect the camera from the laser light and reflections from the channel, while most of the fluorescent light from the seeding particles could pass through. The camera has a matrix of $1,280 \times 1,024$ pixels and a 12-bit intensity resolution. The optical specifications of the system are presented in Table 2.

The numerical aperture (N.A.) of an objective is a measure of the light gathering capacity of the lens system and its ability to resolve details at a fixed object distance. The N.A. is determined by the following formula:

$$\text{N.A.} = n \sin \theta \quad (7)$$

where n is the refractive index of the medium between the imaging point and the objective, and θ is the vertex angle of the largest cone of light refracted from the imaging point

Table 2 Specifications of the optical system

Magnification (M)	Numerical aperture (N. A.)	Lens resolving power (ϵ)	Theoretical pixel resolution
2.5	0.18	2.0 μm	2.7 μm
Lens focal depth	Total pixel focal depth (d)	Field of view	Experimental pixel resolution
9.0 μm	24 μm	2.7 mm	2.6 μm

(i.e. half the angular aperture). The resolving power of a lens (ε) can be defined as its ability to allow the viewer to distinguish between two lines or points in an object. The Raleigh formula is generally used to calculate the resolving power:

$$\varepsilon = 0.61 \frac{\lambda}{\text{N.A.}} \quad (8)$$

where λ is the wavelength of the light, which in this study can be approximated to that of the emission peak (584 nm) of the light scattered by the seeding particles. The resolving power is thus 2 μm and is the smallest distance between two points or lines that can still be distinguished in an image. The total focal depth (d) is calculated using the Berek formula (Innings and Trägårdh 2005):

$$d = 0.5 \frac{\lambda}{(\text{N.A.})^2} + \frac{\text{Sensor resolving power}}{\text{N.A.} \times M} \quad (9)$$

where M is the magnification. The first term in Eq. 3 is the theoretical lens focal depth and the second term is the maximum unsharpness that is acceptable to the viewer, i.e. the ability to focus changes in a picture. In this case, the sensor resolving power can be approximated to the size of a pixel on the CCD chip. The height of the CCD chip in the camera is 6.9 mm and corresponds to 1,024 pixels, which gives a chip-pixel size of 6.7 μm . The focal depth of 24 μm refers to the distance from the nearest image plane in focus to that of the farthest plane simultaneously in focus. Since the oil drops formed will have a diameter of approximately 1 mm, the images will only show the centre of the drops when focusing on the largest contours of the drop. The concentration of seeding particles was calculated based on an estimated focal depth of 50 μm , because it can be assumed that a particle image 50% out of focus is sharp enough for PIV calculations.

The theoretical pixel resolution in the image is calculated by dividing the chip-pixel size by the magnification. The experimental value of the pixel resolution in the image was determined by a calibration procedure in which a micrometre scale was placed in a beaker with the same width and glass window as the experimental channel and filled with the continuous phase. The reason for the difference between the theoretical and experimental values, 2.7 and 2.6 μm , respectively, is that the theoretical value is calculated with respect to the refractive index of air, while the experimental value is based on the refractive indices of the continuous phase, glass and air. The difference could also be a precision error in the calibration measurement.

The PIV system was controlled by a LaVision hardware timing unit, which triggered the measurements. A double exposure with two separate laser pulses was used for velocity measurements in the oil drop and in the continuous phase. Each exposure was stored in a separate frame but in

the same measurement image. The time interval between the two pulses was 500 μs . This time interval was chosen because the particles move less than one fourth of an interrogation area (IA) inside and around the drop when the IA is 32×32 pixels. All images were stored in a computer using DaVis 6.2 software (LaVision GmbH) for further processing and evaluation.

2.4 Data evaluation

The measurement area was 3.1×2.7 mm, resulting in a pixel size of 2.65 μm in the image. The pixel size can be compared with the resolving power of 2 μm , which means that particles can be separated if they have the size of a pixel. The centre of the opening of the glass capillary transporting the dispersed phase is situated at (0,0) in the images.

2.4.1 Velocity calculations of continuous phase

The images used to calculate the velocity of the continuous phase were pre-processed by subtracting a sliding background with a scale length of 20 pixels. The size of the IA was set to 32×32 pixels with an overlap of 50% using a multi-pass algorithm with decreasingly smaller IA sizes. This resulted in spatial resolutions of 43 μm . The PIV calculations were performed with the cross-correlation velocity algorithm. The images were post-processed with a local median filter (Westerweel 1993) in order to detect spurious vectors. The filter computes a local median vector from the eight neighbouring vectors and compares the middle vector with the calculated median. The middle vector is removed and replaced if it differs by more than 1.3 times the root mean square (RMS) of the median.

2.4.2 Velocity calculations of the dispersed phase

The velocity inside the oil drops was calculated using the cross-correlation algorithm in a rectangle that included the drop. The rectangles were divided into IAs of 16×16 pixels with an overlap of 50%, and processed using a multi-pass algorithm with decreasingly smaller IAs, resulting in a spatial resolution of 21.3 μm . A smaller IA can be used here because of the decrease in light noise compared with the measurements in the continuous phase. This is due to the fact that only the dispersed phase was seeded with particles, which means that the total amount of particles was less in the image, leading to a reduction in light reflection. This is also the reason why pre-processing is not necessary when calculating the vectors inside the oil

drop. The median filter described previously was used for post-processing.

3 Results and discussion

3.1 Velocity profile of the continuous phase

To verify the method, the laminar velocity field of the continuous phase was determined without oil drops before the flow inside and around the drops was investigated. The laminar velocity profile of the continuous phase was calculated using final IA sizes of 32×32 and 64×64 pixels. For the smaller size 90% good vectors were obtained and for the larger size 98% good vectors were evaluated. The difference is mainly due to the low particle image density. The amount of particles added to the continuous phase was calculated to be enough for velocity measurement in IAs of 32×32 pixels. However, the particles within the laser light sheet, but out of focus, emitted light that caused a high background level disturbing the light emitted by the particles in focus. The signal-to-noise ratio in the images is at least 2, but adding more particles would cause an increase in the noise from reflections of particles out of focus and the solution would become more opaque, decreasing the detected signal.

Figure 4 shows the axial velocity profiles in the horizontal and vertical planes of the channel calculated with computational fluid dynamics (CFD). The axial velocity profile in the horizontal plane remains at 99% of its maximum velocity for 20% of the width in a rectangular channel with a height-to-width ratio of 1:4, as was used in this study (Fig. 4a). The channel is wide enough that the boundary effects from the sides on drop formation can be neglected. The axial velocity profile in the vertical plane calculated by CFD confirmed the PIV-measured velocities (Fig. 4b). The cross-flow used in this study gave a wall shear stress of 0.5 Pa and a shear rate of 80/s.

3.2 Velocity inside and around a forming drop

The shear stress at the drop interface and the size of the forces involved can be estimated from the velocity fields inside and around a forming drop. The velocity vectors of the flow inside and around a forming drop while attached to the capillary at six different stages in the formation process can be seen in Fig. 5. The internal motion is circulating in the counter-clockwise direction, with the largest velocity vectors in the upper and right-hand quadrants of the drop. The shear stress arising from the cross-flow of the continuous phase affects the dispersed phase and initiates the vortex motion inside the forming oil drop. When the drop

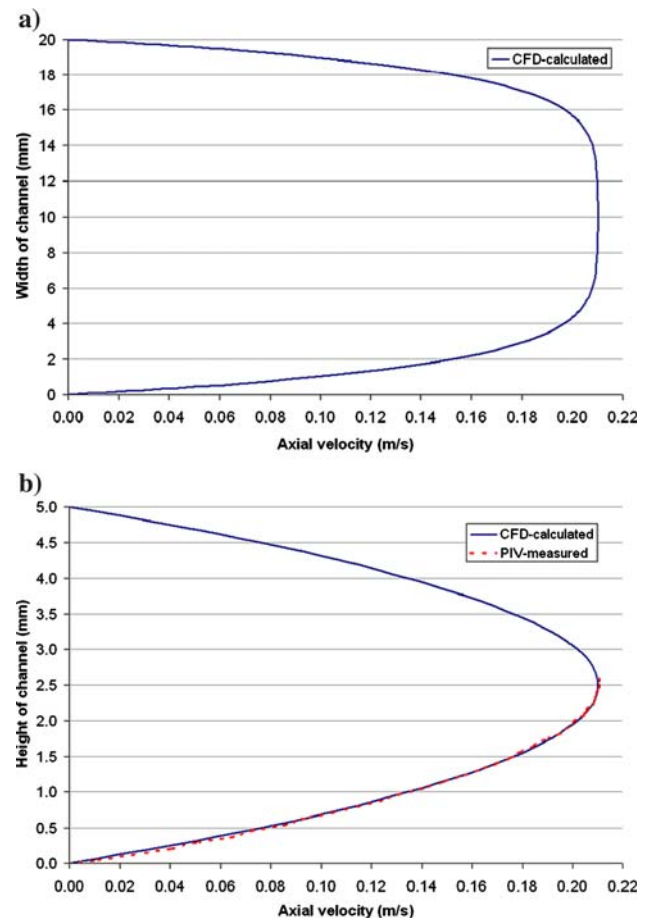
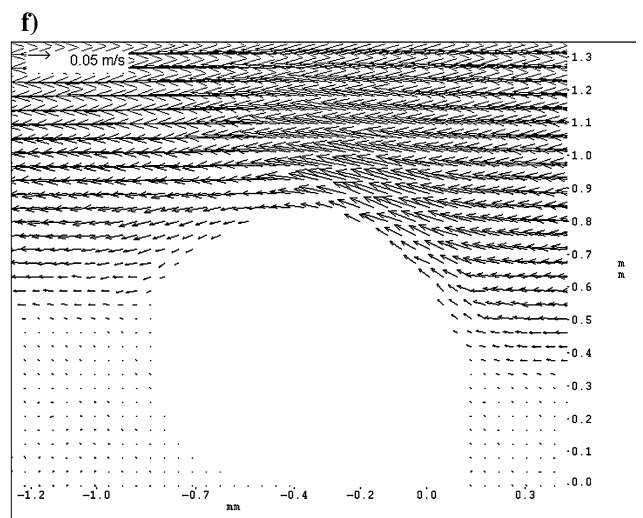
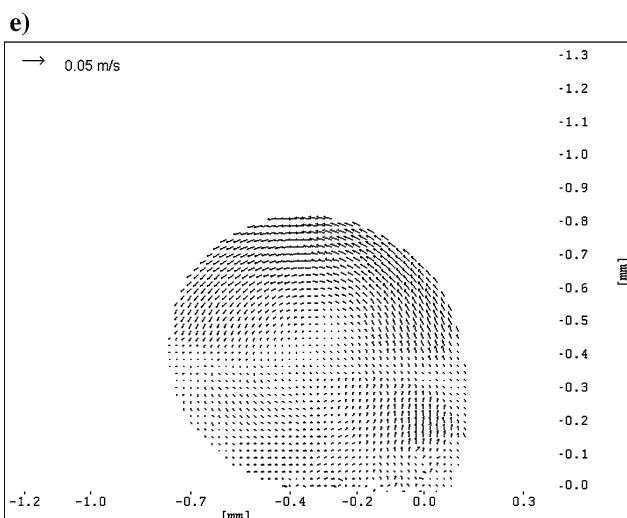
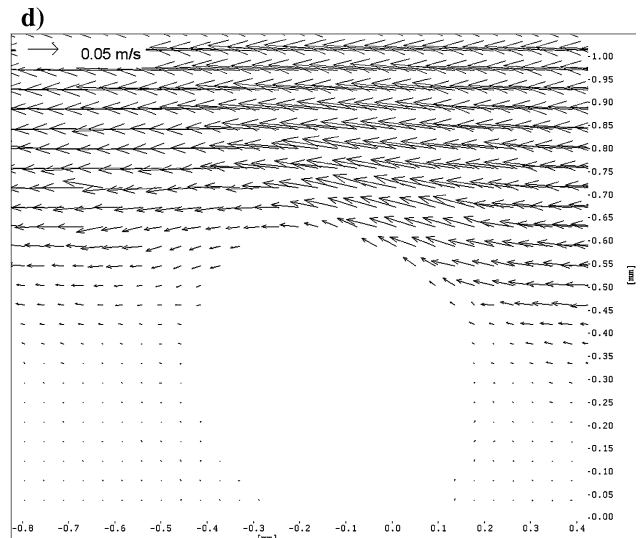
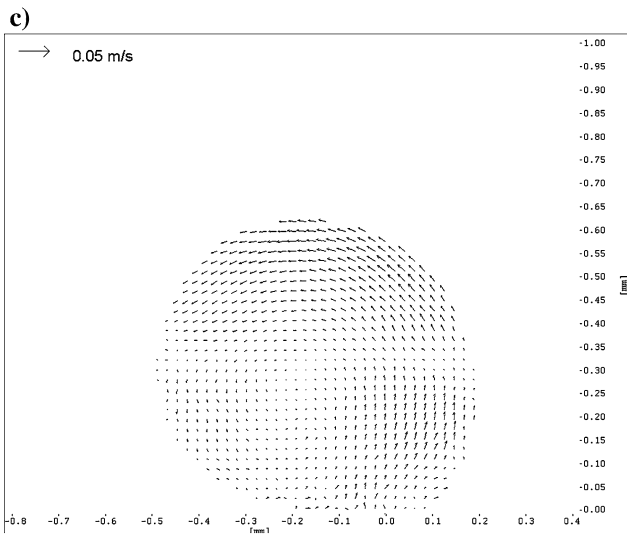
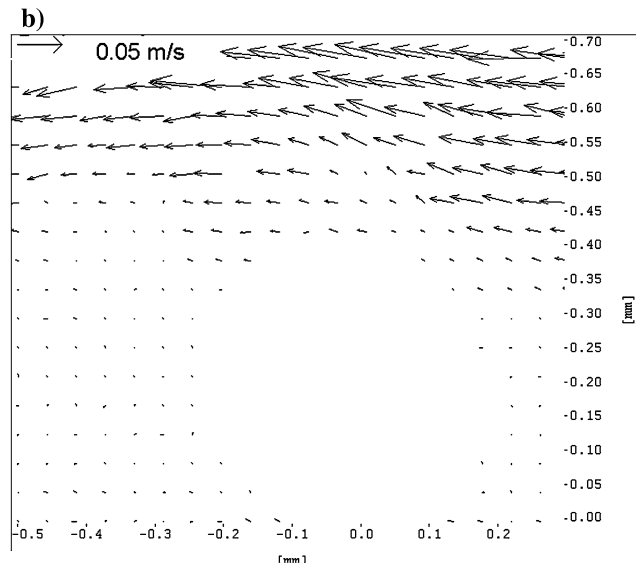
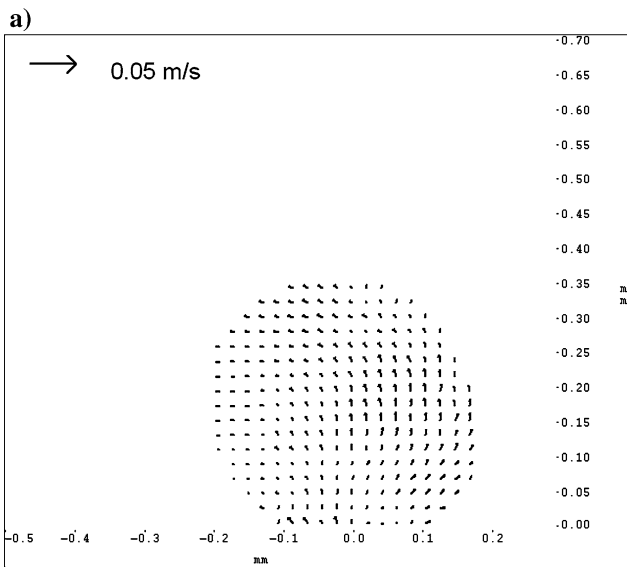


Fig. 4 Velocity profiles for the laminar flow of the continuous phase at an average velocity of 0.11 m/s. The height of the rectangular channel is 5 mm and the width is 20 mm. **a** Shows the CFD-calculated axial velocity profile in the horizontal plane at half the channel height, and **b** the CFD-calculated and PIV-measured axial velocity profile in the vertical plane at half the width of the channel

approaches detachment the circulation point will gradually move towards the left, while the velocity vectors in the upper part of the drop straighten out in the same direction as the cross-flow, as can be seen in Fig. 5k. The influence of the cross-flow on the top of the evolving drop increases as the drop grows and it is thus exposed to a higher cross-flow velocity, which increases the drag force (F_D). This is presented in Fig. 6a, which shows how the main involved forces, calculated with data obtained from the experiment, changes with time during drop formation. These new calculations include the variations in the capillary velocity and

Fig. 5 Velocity vectors when an oil drop is formed at an applied pressure of 90 kPa and the flow of the continuous phase is from right to left with an average velocity of 0.11 m/s (~ 1 drop/s). The *left column* shows the vectors inside the forming drop and the *right column* shows the vectors outside the forming drop. The time and drop diameter are (**a, b**) $t = 0.05$ s, 0.37 mm, (**c, d**) $t = 0.2$ s, 0.65 mm, (**e, f**) $t = 0.43$ s, 0.85 mm, (**g, h**) $t = 0.73$ s, 1.03 mm, (**i, j**) $t = 0.88$ s, 1.13 mm, and (**k, l**) $t = 0.90$ s, 1.15 mm



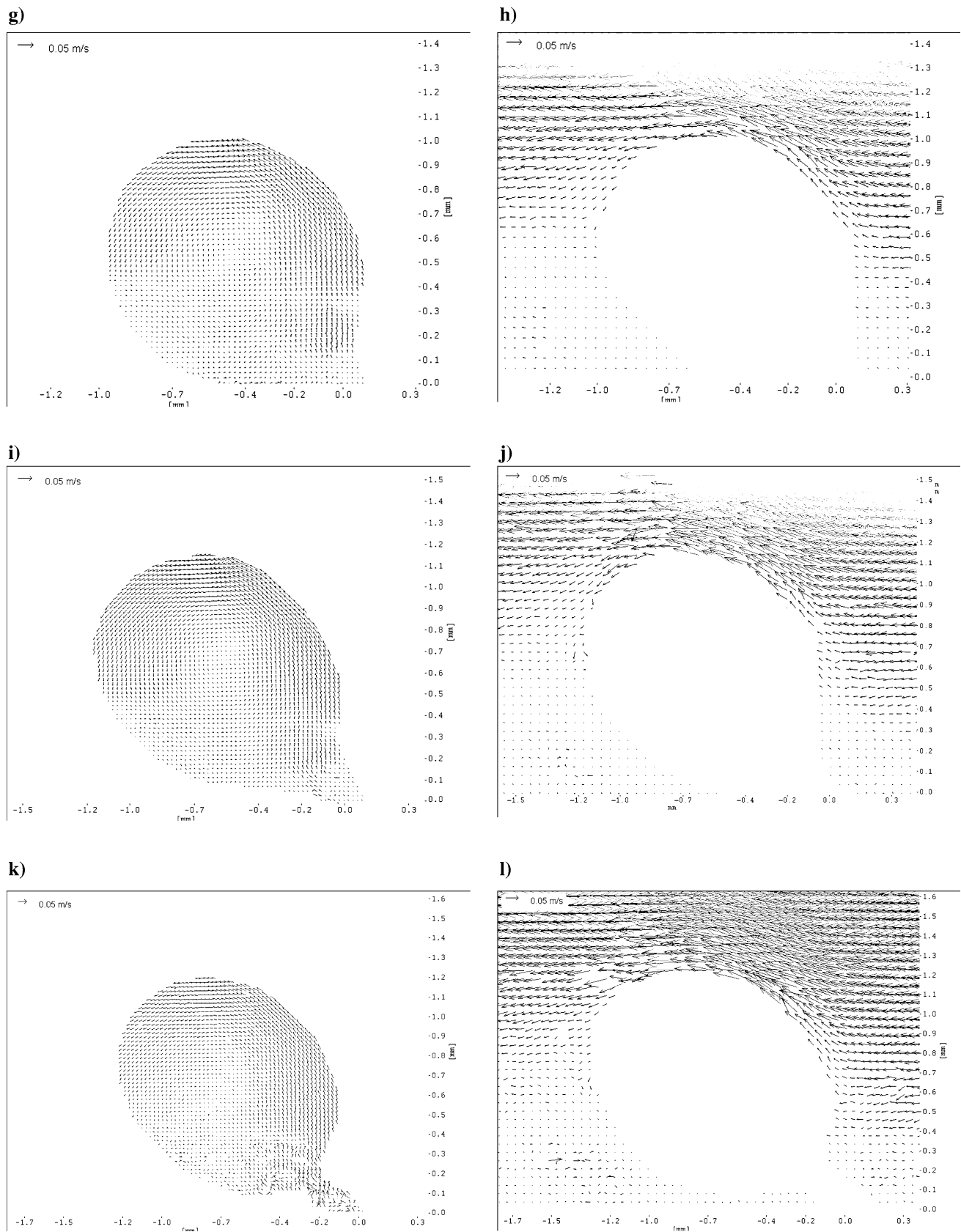


Fig. 5 continued

the neck diameter is used instead of the diameter of the capillary opening in Eqs. 3, 4, 6.

An increasing size of the evolving drop will not only increase the drag force, but also the buoyancy force (F_B) and the lift force (F_L), according to Eqs. 2 and 5. The formation of a neck above the capillary opening will decrease the static pressure force (F_{SP}) and the inertial force (F_I), which promotes the drop to detach. More important is the influence of the formed neck on the decrease of the interfacial tension force (F_γ), which holds the drop to the capillary opening. When the forces promoting detachment, mainly the drag and buoyancy forces, exceed the interfacial tension force holding the drop on the capillary the drop detaches and follows the continuous phase. Figure 6b shows the summation of the involved forces and the diameter of the forming drop as a function of time. The dotted line at 0.8 s in Fig. 6a and b indicates where the detachment forces are equal to the holding surface tension force and the forming drop becomes instable. There is, however, an inertia that delays the detachment.

The flow of the continuous phase follows the contours of the evolving drop until the flow separates from the

interface and forms a vortex behind the drop as can be seen in Fig. 51. The Reynolds number (Re_d), calculated with respect to the curvature of the upstream side of the drop and the free flow velocity in the continuous phase at half the height of the drop, increases to approximately 25 as the drop grows to a final diameter of approximately 1 mm. Deviations from creeping flow will occur at Reynolds numbers (Re) above 20 (calculated with respect to rigid sphere; Clift et al. 1978) and, especially in a case like this, where the evolving drop attached to the capillary opening will be deformed. The deformation and Re_d will increase as the forming drop increases in size (Fig. 5) and the flow begins to form a vortex behind the drop just before detachment (Fig. 51). The formation of the vortex will reduce the pressure behind the drop and thereby increasing the drag. Inertia will also affect flow separation. The ratio of viscosity between the dispersed and continuous phase was 7.2 in the system used, which should result in delayed separation compared with a solid sphere. However, the deformation of the evolving drop while attached to the capillary opening will change the conditions and promote earlier flow separation. Furthermore, internal circulation in the drop can cause deviations in the continuous phase downstream of the drop. Near the interface behind the drop the velocity inside the drop is higher than outside the drop, which results in a local shear from the oil phase to the continuous phase.

The shear stress along the interface can be estimated from the tangential velocity vectors near the interface of the two phases. The shear stress is defined as:

$$\tau = \mu \frac{\partial u}{\partial y} \tag{10}$$

where μ is the dynamic viscosity of the fluid, u the local velocity tangential to the interface and y the distance normal to u . A good estimate is achieved by using the difference between the vectors (Δu) and the distance (Δy) normal to the interface between these vectors, shown in Fig. 5e,f,i,j, in Eq. 10. The distance (Δy) varies from 21 to 30 μm inside and from 42 to 60 μm outside the interface, depending on the gradient of the interface in relation to the grid in the image. The accuracy of the calculations is limited mainly by the pixel resolution and how close to the interface the nearest vector can be determined by the PIV calculations. The nearest accurate velocity vectors used in these calculations can be determined at a distance of 10–60 μm from the interface of the two phases depending on the position of the grid compared to the interface. The largest distance occurs rarely in the continuous phase. The resulting shear stress is presented in Fig. 7, which shows the trend in shear stress around the forming drop. The angle on the horizontal axis is calculated with respect to the centre point of the forming drop, and the centre point is

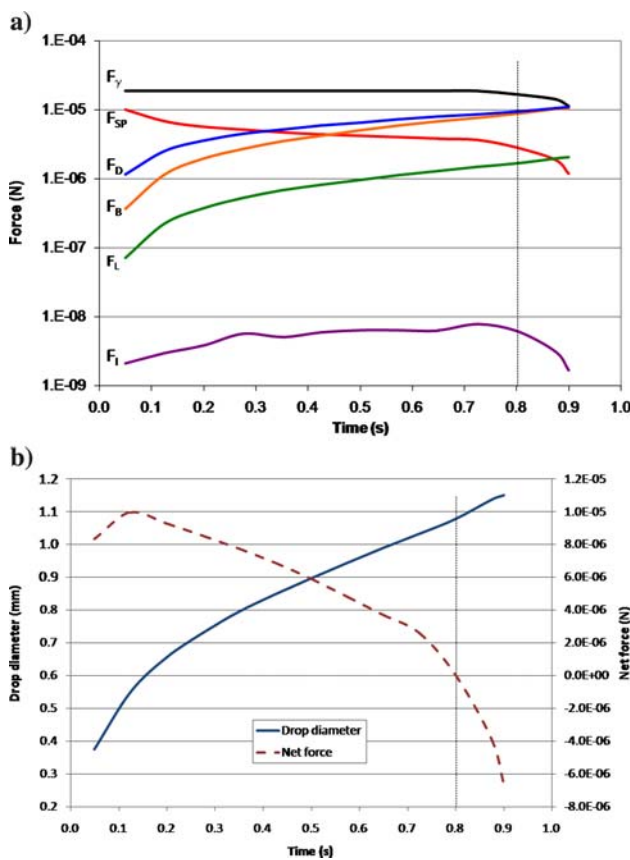


Fig. 6 a Main forces involved in the drop formation process calculated using data from the PIV-measurements. b Summation of the detachment (F_D , F_B , F_L , F_{SP} , F_I) and holding (F_γ) forces. The vertical dotted line indicates time for $\Sigma F = 0$

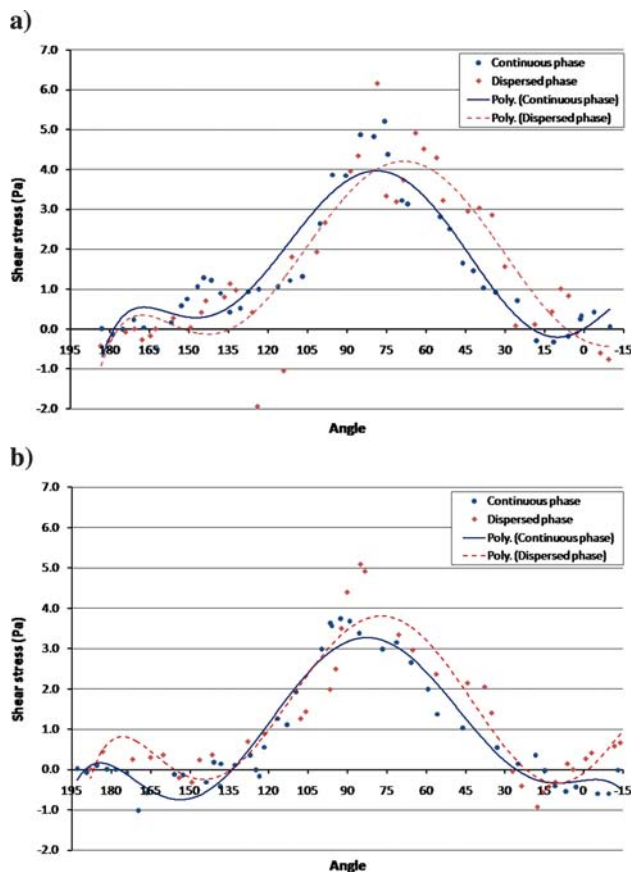


Fig. 7 Shear stress near the interface inside (dispersed phase) and around (continuous phase) a forming drop. The front (*right side*) of the forming drop is at 0° , the *top* at 90° and the back (*left side*) at 180° . The time and drop diameter are **a** $t = 0.43$ s, 0.85 mm and **b** $t = 0.88$ s, 1.13 mm

located at half the height and width in the forming drop. In Fig. 7, a positive shear stress in the continuous phase implies an exerted shear from the cross-flow to the interface whereas a positive shear stress in the dispersed phase means a higher velocity at the interface than further inside the drop. There are two main reasons for the spreading of the data points in Fig. 7: (1) the distance between the interface and the vectors is not constant, and (2) the distance between the vectors varies because the Cartesian distribution of the vectors does not follow the curved interface. The shear stress in the continuous phase fluctuates around zero both upstream of the drop at low angles, and downstream at angles around 180° . The low shear upstream is of course due to the stagnation point where the cross-flow reaches the evolving drop, and the low shear downstream is a consequence of the deviations in the continuous phase behind the drop, presumably caused by the rotational motion inside the drop and by flow separation in Fig. 7b. A reversed shear is reached around 140° in Fig. 7b, which should define the flow separation point at this late stage of drop formation.

Reversed shear stress is also observed in the dispersed phase. At low angles this is caused by the relatively high velocity of the jet from the capillary. The flow of oil into the drop will lead to a higher velocity in the area above the capillary opening than at the interface of the evolving drop. The reversed shear in the dispersed phase above 150° is caused by the irregular flow in the continuous phase, resulting in stagnation in the flow at the interface, which in turn leads to a higher velocity further inside the forming drop. The maximum values of the shear stress are reached around 70° for both the inside and outside of the drop in Fig. 7a and at a slightly higher angle in Fig. 7b since the drop is more deformed at this late stage. The high values of shear stress in the dispersed phase at 60° is because of the centre of the jet of fluid leaving the capillary intersects with the curvature of the interface of the forming drop at this point. The shear stress in the dispersed phase is not only a consequence of the cross-flow, but also highly affected by the momentum transfer caused by the fluid ejected through the glass capillary and liquid rotation inside the evolving drop. However, this observed rotation is due to the effects of the cross-flow and the viscous interactions with the surrounding flow. The shear stress pattern in the cross-flow of the continuous phase is mainly due to the flow past a forming drop and, to a smaller extent, the rotation inside the drop.

4 Conclusions

The aim of this work was to develop a measurement technique that can be used to determine the velocity field inside and around an oil drop, during formation from a single glass capillary with an internal diameter of $200\ \mu\text{m}$, into a laminar cross-flow. A new approach of the PIV technique was used. This included a microscope that gave a narrow focal depth in the centre cross section of the forming drop, which shows that this PIV method is applicable to the measurement of velocities in a liquid–liquid flow, where the volume of interest is in the region between general PIV and micro-PIV, with a pixel resolution of $2.6\ \mu\text{m}$. The measurements showed that the laminar continuous cross-flow induces an internal rotational velocity in the forming oil drop. This cross-flow causes, together with the oil jet out of the capillary, a shear stress at the interface of the drop. A maximum shear stress can be seen at approximately 75° from the stagnation point. The forces involved have been calculated with the achieved data, which can predict the drop formation time. The developed method can provide deeper insight into the physical phenomena occurring during drop formation and detachment in a two-phase system. The results will also be valuable to validate future numerical simulations.

Acknowledgments This work was financially supported by the Swedish Research Council.

References

- Abrahamse AJ, van Lierop R, van der Sman RGM, van der Padt A, Boom RM (2002) Analysis of droplet formation and interactions during cross-flow membrane emulsification. *J Membr Sci* 204:125–137
- Augier F, Masbernat O, Guiraud P (2003) Slip velocity and drag law in a liquid–liquid homogeneous dispersed flow. *AIChE J* 49:2300–2316
- Clift R, Grace JR, Weber ME (1978) Bubbles, drops and particles. Academic Press, New York, p 102
- Crowe CT, Sommerfeld M, Tsuji Y (1998) Multiphase flows with droplets and particles. CRC, New York, p 24
- Innings F, Trägårdh Ch (2005) Visualization of the drop deformation and break-up process in a high pressure homogenizer. *Chem Eng Technol* 28:882–891
- Kobayashi I, Yasuno M, Iwamoto S, Shono A, Satoh K, Nakajima M (2002) Microscopic observation of emulsion droplet formation from a polycarbonate membrane. *Coll Surf Physicochem Eng Aspects* 207:195–196
- Koutsiaris AG, Mathioulakis DS, Tsangaris S (1999) Microscope PIV for velocity-field measurement of particle suspensions flowing inside glass capillaries. *Meas Sci Technol* 10:1037–1046
- Lindken R, Di Silvestro F, Westerweel J, Nieuwstadt FTM (2002) Turbulence measurements with μ -PIV in large-scale pipe flow. In: Proceedings of the 11th international symposium on applications of laser techniques to fluid mechanics, Paper 12.1, Lisbon, 8–11 July 2002
- Milosevic IN, Longmire EK (2002) Pinch-off modes and satellite formation in liquid/liquid jet systems. *Int J Multiphase Flow* 28:1853–1869
- Mohamed-Kassim Z, Longmire EK (2003) Drop impact on a liquid–liquid interface. *Phys Fluids* 15:3263–3273
- Mohamed-Kassim Z, Longmire EK (2004) Drop coalescence through a liquid/liquid interface. *Phys Fluids* 16:2170–2181
- O’Neill ME (1968) A sphere in contact with a plane wall in a slow linear shear flow. *Chem Eng Sci* 23:1293–1298
- Peng SJ, Williams RA (1998) Controlled production of emulsions using a crossflow membrane Part 1: droplet formation from a single pore. *Trans IChemE* 76:894–901
- Santiago JG, Wereley ST, Meinhart CD, Beebe DJ, Adrian RJ (1998) A particle image velocimetry system for microfluidics. *Exp Fluids* 25:316–319
- Svensson FJE, Rasmuson A (2004) LDA-measurements in a stirred tank with liquid–liquid system at high volume percentage dispersed phase. *Chem Eng Technol* 27:335–339
- Van der Graaf S, Schroën CGPH, van der Sman RGM, Boom RM (2004) Influence of dynamic interfacial tension on droplet formation during membrane emulsification. *J Colloid Interface Sci* 279:277–280
- Wang Z, Wang S, Schröder V, Schubert H (2000) Effect of continuous phase viscosity on membrane emulsification. *Chin J Chem Eng* 8:108–112
- Westerweel J (1993) Particle image velocimetry—theory and application. Ph.D. Thesis. Delft University Press
- Westerweel J (2000) Theoretical analysis of the measurement precision in particle image velocimetry. *Exp Fluids (Suppl)*: S3–S12
- Westerweel J, Geelhoed PF, Lindken R (2004) Single-pixel resolution ensemble correlation for micro-PIV applications. *Exp Fluids* 37:375–384
- Xu JH, Luo GS, Chen GG, Wang JD (2005) Experimental and theoretical approaches on droplet formation from a micrometer screen hole. *J Membr Sci* 266:121–131
- Yasuno M, Nakajima M, Iwamoto S, Maruyama T, Sugiura S, Kobayashi I, Shono A, Satoh K (2002) Visualization and characterization of SPG membrane emulsification. *J Membr Sci* 210:29–37